High-efficient catalysts of core-shell structured Pt@transition metal oxides (TMOs) supported on 3DOM-Al$_2$O$_3$ for soot oxidation: The effect of strong Pt-TMO interaction

Qiangqiang Wu[1], Meizan Jing[1], Yuechang Wei*, Zhen Zhao, Xindong Zhang, Jing Xiong, Jian Liu, Weiyu Song, Jianmei Li

State Key Laboratory of Heavy Oil Processing, College of Science, China University of Petroleum, Beijing 102249, China

ABSTRACT

Diesel soot particles are important components of atmospheric fine particles, and the key factor in controlling soot emissions is the performance of catalysts in after-treatment systems. Herein, a series of high-efficient nanocatalysts of Pt@transition metal (Mn, Fe, Co, Ni, Cu) oxides (TMOs) core-shell nanoparticles (NPs) supported on 3D ordered macroporous (3DOM) Al$_2$O$_3$ (Pt@TMO/3DOM-Al$_2$O$_3$) were designed and synthesized. The strong Pt-TMO interaction at the optimized interface of Pt@TMO core-shell NPs induces the formation of coordination unsaturated active sites for activated reactants (O$_2$ and NO). Pt@TMO/3DOM-Al$_2$O$_3$ catalysts exhibit high catalytic activity dependence on the strong Pt-TMO interaction for soot oxidation, and Pt@CoO$_x$/3DOM-Al$_2$O$_3$ catalyst shows the highest catalytic activity (T$_{50}$ = 357 °C, TOF = 2.76 S^{-1} ×10^{-3}) and the lowest apparent activation energy (52 kJ mol^{-1}) in the presence of O$_2$ (5%), NO (0.2%) and H$_2$O (5%). In addition, Pt@TMO/3DOM-Al$_2$O$_3$ catalysts exhibit excellent H$_2$O and SO$_2$ resistances during catalytic soot oxidation. Based on the results of characterizations and density functional theory calculations, the coordination unsaturated Co-based active sites have efficient catalytic performance for NO oxidation to NO$_2$ intermediate, which is an important reaction pathway for catalytic soot oxidation. Insight into the activity dependence on the strong Pt-TMO interaction is not only meaningful for development of advanced catalysts, but also supports the development of Pt@TMO nanoparticles for practical applications of emission reduction of diesel soot.

1. Introduction

Particulate matter (PM) emissions from diesel engines, consisting mainly of soot particles, can cause serious atmospheric environmental and human health problems [1]. Diesel soot particles need to be eliminated or reduced by efficient exhaust treatment techniques. One of the most efficient after-treatment techniques for soot reduction in diesel exhaust is combination of the use of oxidation catalysts and diesel particulate filters (CDPF) [2]. A number of catalysts with good performance for soot oxidation have been reported, such as noble metals [3–5], transition metal oxides [6–9], alkaline metal oxides [10,11], perovskite-type oxides [12,13] and rare earth oxides [14–16]. Platinum (Pt) is still primary active component of commercial catalysts for vehicle exhaust purification. Currently, both the effective utilization of Pt component and the achievement of high catalytic activity at diesel exhaust gas temperatures (150–400 °C) remain a challenge.

To design and produce high-performance catalysts for soot oxidation, the primary task is understanding of the nature of catalytic soot oxidation reaction, which is a complex heterogeneous catalysis that occurs at three-phase boundary involving solid soot particle, solid catalyst and gaseous reactants (O$_2$, NO) [17]. Thus, the catalytic activity for soot oxidation is affected by two factors: the contact efficiency between active sites of the catalyst and soot; and the density and nature of active sites [18–21]. The structure characteristics of catalysts at nanometer level play an important role in deep oxidation reactions, such as the nanostructure and morphology of oxide supports, and the surface property and size of supported nanoparticles [22,23]. On the one hand, to increase soot-catalyst contact efficiency, macroporous nanostructure materials are used in the field of soot oxidation [24,25]. In our previous work, three-dimensionally ordered macroporous (3DOM) catalysts with uniform pore sizes (> 50 nm) can improve the contact efficiency between soot and catalyst and enhance mass transfer

---

of soot particles, thus they exhibited higher catalytic performance for diesel soot oxidation compared to the nanoparticle and disordered macroporous materials [21].

On the other hand, it was also found that the catalytic performances are related to the adsorption and activation properties of active sites for O_2 and NO, which are located at the interface between noble metal and metal oxides [26–30]. As reported by Q. Fu [31], the active sites for O_2 activation are coordination unsaturated Fe sites located at the interface between Pt and iron oxides during the CO oxidation. The performance of Pt catalyst can be further improved by controlling the interface structure between Pt and oxide with strong metal-support interaction (SMSI) [32–34]. The preferred method to optimize metal-oxide active interface areas is to support noble metal (core) and oxide (shell) nanoparticles with unique structures [35]. The nanocatalysts of Pt@ oxides core-shell nanoparticles show superior catalytic properties unattainable by their single counterparts, and they improve the effective utilization of the Pt component [36–38]. However, in-depth research on the strong interaction between Pt and transition metal (TM: Mn, Fe, Co, Ni, Cu) oxides (TMOs) in enhancing catalytic activity has not been reported in the literature. Thus, fabrication of Pt@TMO core-shell nanoparticles on 3DOM supports provides an effective means to investigate the catalytic activity-dependent Pt-TMO interaction during soot oxidation.

In terms of both effective utilization of Pt component and enhancing catalytic activity, ideal strategy is to combine the optimized Pt-oxides interface areas with enhancing catalyst-soot contact efficiency. Herein, we have designed and synthesized the novel nanocatalysts of Pt@TMO core-shell nanoparticles supported on 3DOM Al_2O_3 via gas bubbling-assisted membrane reduction-precipitation (GBMR/P) method [39]. The effect of the strong Pt-TMO (Mn, Fe, Co, Ni, Cu) interaction on catalytic activity during soot oxidation was investigated by the characterizations and density functional theory (DFT) calculations. Pt@CoO$_x$/3DOM-Al$_2$O$_3$ catalyst shows the highest catalytic activity for soot oxidation, and the catalytic pathway of NO oxidation to NO_2 intermediate is rate determining step for soot oxidation. Pt@TMO/ 3DOM-Al$_2$O$_3$ catalysts are not only an excellent and heritable system for soot oxidation, but they are also model catalysts for heterogeneous catalytic reaction.

2. Experimental sections

2.1. Synthesis of Pt@TMOs (TM: Mn, Fe, Co, Ni, Cu)/3DOM-Al$_2$O$_3$ catalysts

3DOM Al_2O_3 support was synthesized by colloidal crystal template (CCT) method, which consists of four steps: (i) Synthesis of monodispersed PMMA microspheres with an average diameter of 400 ± 50 nm and assembly of PMMA microspheres by centrifuge method to CCT; (ii) Impregnation of precursor solution into dried PMMA colloidal crystal templates, and the removal of the excess solutions via filtration; (iii) The removal of CCT by calcination in an air flow of 80 ml min^{-1} at a slope of $1\,°C\,min^{-1}$ from room temperature to 650 °C. Finally, 3DOM Al_2O_3 support was obtained. The detailed processes are shown in *Supporting Information*.

Pt@TMO/3DOM-Al$_2$O$_3$ catalysts were prepared by GBMR/P method, and the schematic diagrams of GBMR/P method are illustrated in detail in Figure S1. Typical synthetic procedures were divided into two steps: GBMR and GBMP steps. For GBMR step, the suitable amounts of 3DOM Al_2O_3 support was dispersed in deionized water (200 ml) under magnetic stirring at room temperature, and a stabilizer (Poly *N*-vinyl-2-pyrrolidone, 1.1 g) and the stoichiometric amount of H_2PtCl_6 solution (theoretical Pt loading 4 wt %) were then added into above solution (denoted as Beaker I) dropwise with agitation. The pH value of mixture solution is ∼3.0 by the adjustment of HCl solution, which is lower than the isoelectric point (IEP) of Al_2O_3 support. A cycling flow of above mixture solution between membrane reactor and Beaker I was

carried out through a peristaltic pump at a flow rate of 360 ml min^{-1}. In the membrane reactor, the mixture solution flowed in the glass tube and outside the ceramic tubes. NaBH$_4$ solution (50 ml, molar ratio of [NaBH$_4$]/[Pt] of 5) was introduced into the above solution through abundant holes (d = 40 nm) on the walls of ceramic tubes at a constant flow rate of 1.0 ml min^{-1}. Meanwhile, a gas-bubble-assisted stirring operation was developed to stir the mixture solution through two other ceramic tubes, and the reaction system was bubbled with hydrogen gas (40 ml min^{-1}). Pt/3DOM-Al$_2$O$_3$ catalyst was obtained. For the GBMP step, Pt/3DOM-Al$_2$O$_3$ and TM (Mn, Fe, Co, Ni, Cu) nitrates (molar ratio of [TM]/[Pt] is 3) were mixed and introduced into a beaker (150 ml). Precipitation agent (NH$_3$·H$_2$O) was then added into the membrane reactor, as in GBMR process. The synthesis process was stopped after running out of precipitation agent. Then, the sample was filtered and washed with deionized water until no Cl- via the detection of using an AgNO$_3$ solution. The solid was dried in an oven at 60 °C for 12 h, and further calcined in an air atmosphere at 550 °C for 4 h to remove H$_2$O and stability reagent. Finally, desired Pt@TMO/3DOM-Al$_2$O$_3$ catalysts were obtained.

2.2. Characterizations

Physicochemical characteristics of all the catalysts, including nanostructures and surface properties, were determined using techniques such as scanning electron microscopy (SEM), transmission electron microscopy (TEM), X-ray diff;raction (XRD), N_2 adsorption/desorption, hydrogen temperature-programmed reduction (H$_2$-TPR), X-ray photoelectron spectroscopy (XPS), inductive coupled plasma optical emission spectrometry (ICP-OES) and NO temperature-programmed oxidation (NO-TPO). The surface morphology of the samples was investigated by means of a field emission SEM on a Quanta 200 F instruments operating at 5 kV. TEM and HRTEM images were recorded on JEO1 JEM 2100 electron microscope equipped with a field emission source, operating at an accelerating voltage of 200 kV. The average particle diameter (d) of all samples was calculated by the following equation: d = Σnidi/Σni, where ni is the number of particle diameter (di) in a certain range, and Σni is more than 100 particles on transmission electron microscope images of the sample. Powder XRD measurements were recorded on a X-ray diffractometer (Shimadzu XRD 6000) operating at 10 mA and 40 kV using Cu Kα radiation (λ = 0.15406 nm, 4° min^{-1} from 20 to 90°) with a Nickel filter. XRD patterns were compared with JCPDS reference data to explore the phase identification of samples. The crystallite sizes of Al_2O_3 samples were calculated from the half-height width of (440) crystal face peak using the Debye-Scherrer equation: $D (hkl) = 0.89\lambda./(\beta cos\theta)$, where λ is the wavelength of radiation, β is the corrected peak width at half-maximum intensity (FWHM), and θ is the peak position.

Nitrogen adsorption/desorption isotherm was performed on an automated gas sorption analyzer (Quantachrome Autosorb-iQ, USA) at -196 °C. The samples have degassed for 4 h at 300 °C to remove water and other atmospheric contaminants before experiments. The specific area was determined from Brunauer-Emmett-Teller (BET) equation in 0.05-0.3 relative pressure (P/P$_0$) range, and pore-size distribution was obtained by BJH method using desorption branch. H$_2$-TPR measurements were carried out on a conventional flow apparatus equipped with a thermal conductivity detector (TCD) to monitor the consumption of hydrogen, and a cooling trap and a filter packed with molecular sieve 5 A (60–80 meshes) were used to remove H$_2$O and CO_2 before outlet gases entering TCD. The sample (100 mg) was pretreated in an air atmosphere at 200 °C for 1 h, and then cooled to 30 °C with Ar. H$_2$-TPR analysis was performed by heating the pretreated sample from 30 to 900 °C with a heating rate of 10 °C min^{-1} under an mixture gas flow (10% molar H$_2$ in Ar, 40 ml min^{-1}). XPS studies were taken on a PerkinElmer PHI-1600 ESCA spectrometer using a Mg Kα X-ray excitation source. XPS analyses were performed at ambient temperature, and the pressure in the vacuum chamber during the test was less than

10^{-7} mbar. Prior to analysis, the catalysts were outgassed under vacuum for 4 h. The binding energies were referenced to C1s peak of contaminant carbon (BE = 284.6 eV) to revise the shift caused by charge effect. The actual content of Pt in all samples was determined by ICP-OES (PE, OPTIMA 5300DV). Temperature-programmed oxidation experiments of NO were carried out on the fixed beds for studying on the formation of NO_2. Reactant gas compositions were 5% O_2 and 0.2% NO with He balanced gas. The reaction temperature ranged from 100 to 500 °C. The catalyst was 100 mg and without soot during the reaction. The other reaction conditions were the same as following soot-TPO experiment. NO_2 concentration in the outlet gas was in situ detected by mass spectrometry (MS, Quantachrome autosorb-1C).

2.3. Catalytic activity evaluation

Catalytic activities of all catalysts for soot oxidation were evaluated by soot-temperature programmed oxidation (soot-TPO) on a fixed-bed tubular quartz system (φ = 8 mm) from 150 to 650 °C at a heating rate of 2 °C min^{-1}. The reaction temperature was accurately measured by a thermocouple placed close to the middle of catalytic bed. Commercially available carbon particles (Printex-U, Degussa, Germany) were used as model soot in this study. Catalyst (100 mg) and soot (10 mg) were mixed using a spatula to simulate loose contact packing. Reactant gas flow (50 ml min^{-1}) contained 5 vol % O_2, 0.2 vol % NO and 5 vol % H_2O or 0.02 vol % SO_2, and the remainder was Ar. An on-line gas chromatograph (GC, Sp-3420, Beijing) with a flame ionization detector (FID) was employed to monitor the concentrations of CO (C_{CO}) and CO_2 (C_{CO2}) in the outlet gas. Total amounts of CO and CO_2 products (T_C) were obtained by numerical intergration with the equation: $T_C = \int [C_{CO} + C_{CO2}]$ (%) × 50 (mL min^{-1}) × dT (min), and T is total time during soot oxidation. Based on the rising temperature rate of 2 °C min^{-1} and starting temperature at 150 °C in soot-TPO experiments, the instantaneous amounts of CO and CO_2 products (I_C) at each sampling points (°C) can be calculated by numerical intergration with the equation: $I_C = \int [C_{CO} + C_{CO2}]$ (%) × 50 (mL min^{-1}) × dt (min), and t is the time from 150 °C to each sampling points. Catalytic activity was evaluated at the temperature values (T_{10}, T_{50}, and T_{90}) for achieving soot conversion of 10%, 50% and 90% obtained by the percent of I_C/T_C × 100%, respectively. The selectivity to CO_2 formation (S_{CO2}) was defined as the C_{CO2} divided by the sum of C_{CO2} and C_{CO}. S_{CO2}^m was denoted as the S_{CO2} at which C_{CO2} value was the maximum.

Apparent turnover frequency (TOF) was taken as parameters of catalytic activity and utilization efficiency of Pt atoms during soot oxidation, which was defined as the ratio of reaction rate to amount of ionic $Pt^{\&+}$ species in catalysts. On the one hand, the reaction rates (R) of catalysts were obtained through isothermal reaction for soot oxidation. The temperature of isothermal reaction was selected at 300 °C in an approximate kinetic regime due to the conversion of soot oxidation was low and nearly constant over time, and the reaction was conducted under conditions of 5 vol% O_2, 0.2 vol% NO and 5 vol % H_2O balanced by Ar using a total flow rate of 50 ml min^{-1}. Furthermore, in order to exclude internal and external mass transport diffusion and heat transfer, a series of procedures were performed, such as the small particle diameter (< 40 μm) of catalysts and the relatively high flow rate. On the other hand, active site density of Pt@TMO/3DOM-Al_2O_3 catalysts was calculated according to the amounts of ionic $Pt^{\&+}$ species determined by the results of XPS and ICP-OES. Finally, TOF_{Pt} kinetic measurements for soot oxidation were obtained. The apparent activation energy (E_a) of soot oxidation reaction was measured via the Ozawa method from soot conversion data [40]. The soot-TPO measurement was carried out at different heating rates (Φ) of 2, 4, 6 and 10 °C min^{-1}. The value of absolute temperature (T_α), at which a fixed fraction (α) of soot was combusted for each heating rate, was obtained from the soot conversion curve. The activation energy was calculated from the least squares fit of logΦ versus T_α^{-1} data series, using the following equation: logΦ = B-0.4567(E_α/RT_α), where B is a constant value with regards to

the reaction.

2.4. Density functional theory (DFT) calculations

To determine reaction pathways of NO_x-assisted soot oxidation over supported Pt(111)@TMO catalysts, all the spin-polarized DFT calculations were performed using the Vienna Ab initio Simulation Package (VASP) code based on the all-electron projected augmented wave (PAW) method and on a plane wave basis set [41]. Detailed DFT calculation procedures are described in the *Supporting Information*. Taking into account the lattice mismatch between TMOs and Pt, TMOs nano-island covered (2 $\sqrt{3}$ × 5) rectangular supercell (three Pt(111) metal layers with lattice constants of 2.82 Å) were applied with 3 × 2 × 1 k-point sampling. TMO nano-islands consisted of three TMs and three O columns coordinated with the top layer of the Pt substrate. During the structural optimization, bottom two Pt layers and one TM-O column were frozen as indicated in Figure S2, while the remaining atoms were all relaxed. The vacuum space was set to 15 Å. For comparison, the model of bare Pt(111) surface was constructed by using a five-layer p (3 × 3) Pt(111) slab with 3 × 3 × 1 k-point sampling [42]. In addition, all microkinetics simulations were performed using MKMCXX software. Rate constants of the elementary reaction steps are used within mean filed differential equations describing the kinetics of each reaction to model the kinetics of the entire reaction network. For surface reactions, the rate constants for the forward and backward elementary reactions were determined by the Eyring equation detailed in *Supporting Information*.

3. Results

3.1. SEM and TEM images

The morphology and macroporous structure of Pt@TMO/3DOM-Al_2O_3 catalysts were revealed by SEM and TEM images, and the results are shown in Fig. 1. As shown in Fig. 1(A1-E1), Pt@TMO/3DOM-Al_2O_3 catalysts have a well-defined, long-range 3DOM structure, which is similar to 3DOM Al_2O_3 support (Figure S3) and Pt/3DOM-Al_2O_3 catalyst (Figure S4). It indicates that the synthesis method (GBMR/P) of Pt@TMO/3DOM-Al_2O_3 catalysts did not cause significant modification in 3DOM architecture. Uniform close-packed periodic voids with a pore-size range of 270–320 nm were observed, which is in agreement with the shrinkage of 30–40 % in comparison with original size (400 ± 50 nm) of PMMA microspheres (Figure S5). It is related to the complete removing of PMMA colloidal crystal templates at a higher temperature and the formation of metal oxide crystals. The next layer of macropores can be clearly observed, and the periodic voids are interconnected through a pore window, with a diameter of 85 ± 5 nm. The high connectivity of ordered macropores is favorable for soot particles mass transfer, which could allow soot particles easily to contact active sites on the surface of inner macropore wall because macropore diameter is larger than particle diameter of soot (> 25 nm).

The nanostructures of Pt@TMO/3DOM-Al_2O_3 catalysts were further investigated by TEM and HRTEM images. As shown in Fig. 1(A2-E2), all the catalysts exhibited an overlapped ordered macroporous structure, which is similar to pore structure of Pt/3DOM-Al_2O_3 catalyst, with an average pore diameter of 300 nm (Figure S6). The periodic macropores are interconnected via open windows (85 ± 5 nm), which is supported by the results of SEM images. 3DOM structure is an ideal reaction site that can improve contact efficiency between soot and catalysts because soot particles are permitted inside of 3DOM catalysts. Therefore, the catalytic performance of 3DOM catalysts for soot oxidation will be improved remarkably. As shown in the inset of Fig. 1(A2), the crystal structure of catalyst is investigated by selected area electron diffraction (SAED) pattern. The characteristic rings of SAED pattern from interior to exterior are indexed as Pt(111) and Al_2O_3(400) crystal faces.

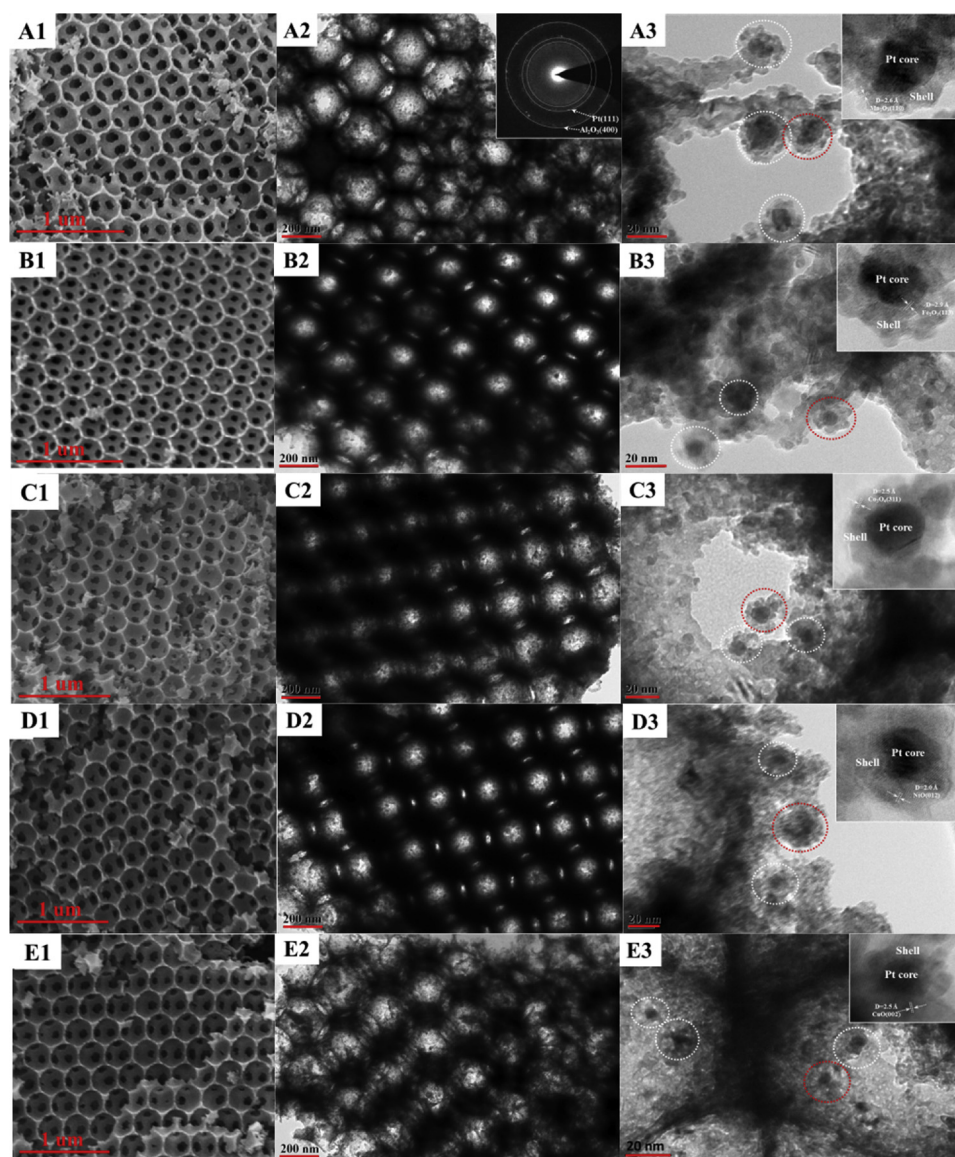Based on the contrast of Pt, TMO and Al_2O_3 in TEM images,

Fig. 1. SEM (A1-E1), TEM (A2-E2) and HRTEM (A3-E3) images of Pt@TMO/3DOM-Al₂O₃ catalysts. (A) Pt@MnOₓ/3DOM-Al₂O₃, (B) Pt@FeOₓ/3DOM-Al₂O₃, (C) Pt@CoOₓ/3DOM-Al₂O₃, (D) Pt@NiOₓ/3DOM-Al₂O₃, (E) Pt@CuOₓ/3DOM-Al₂O₃.

supported Pt@TMO core-shell nanoparticles on the inner wall of 3DOM Al₂O₃ can be clearly observed in Fig. 1(A3-E3). By means of statistical analyses of more than 100 nanoparticles in each sample, particle sizes of Pt (core) have a narrow distribution in the range 3–7 nm and the mean diameter of Pt is about 4.6–5.0 nm, while the thicknesses of shell layers are 2–4 nm. The configuration of TMO shell is a nanoparticle or an isolated island coated on the surface of Pt core, with the thickness of shell layer equals to 8–15 atomic layers. Furthermore, the interplanar spacings of Pt core and TMO shell were distinctly observed, indicating that both Pt core and TMO shell were well-crystallized in the process of preparation. As shown in the inset of Fig. 1(A3-E3), the interplanar crystal spacings of TMO shells are 2.6, 2.9, 2.5, 2.0 and 2.5 Å, which can be assigned to the crystal planes of Mn_2O_3 (110), Fe_2O_3 (113), Co_3O_4 (311), NiO (012) and CuO (002), respectively. The surface lattice distortion of Pt core is also shown in the inset of Fig. 1(A3), which is ascribed to the radius contraction of Pt atoms as a result of the strong interaction between Pt core and TMO shell. The formation of oxide (shell)-Pt (core) nanostructure is strongly related to the nature of the interaction between Pt and TMO. Pt@TMO core-shell nanostructure with optimal strong metal(Pt)-support(TMO) interaction is beneficial to improve the mobility of lattice oxygen in TMO shell and conducive to

the formation of active sites for O_2 and NO activation, which can improve the catalytic activity for diesel soot oxidation.

3.2. XRD spectra and N_2 adsorption-desorption isotherms

Phase structures of 3DOM-Al₂O₃ and Pt@TMO/3DOM-Al₂O₃ catalysts were investigated by means of XRD, and the results are shown in Fig. 2. For 3DOM-Al₂O₃ support, all the symmetric diffraction peaks (2θ) at 37.6, 39.5, 45.7 and 67.0° can be indexed to (311), (222), (400) and (440) crystal planes of a gamma (g) phase of Al₂O₃ with cubic structure (JCPDS PDF# 10-0425), respectively. With the combination observations of no significant difference in peak types and all samples have the symmetric diffraction peaks, indicating that Al₂O₃ support possess single-phase crystal structure. Pt/3DOM-Al₂O₃ catalyst exhibits a strong diffraction peak (2θ) at 39.9° and one weak diffraction peak (2θ) at 81.3°, which are assigned to the (111) and (311) crystal planes of Pt nanoparticles (JCPDS PDF# 70–2057), respectively. And two shoulder peaks located at 46.2 and 67.5° can be observed obviously which are attributed to (200) and (220) crystal faces of Pt nanoparticles, respectively. After TMO nanoparticles deposition on the surface of Pt/3DOM-Al₂O₃ catalyst, the intensities of diffraction peaks
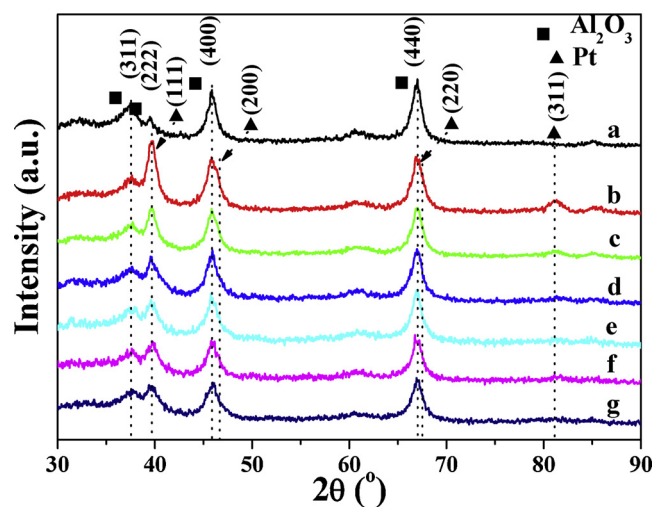
Fig. 2. XRD patterns of 3DOM Al$_2$O$_3$, Pt/3DOM-Al$_2$O$_3$ and Pt@TMO/3DOM-Al$_2$O$_3$ catalysts. (a) 3DOM-Al$_2$O$_3$, (b) Pt/3DOM-Al$_2$O$_3$, (c) Pt@MnO$_x$/3DOM-Al$_2$O$_3$, (d) Pt@FeO$_x$/3DOM-Al$_2$O$_3$, (e) Pt@CoO$_x$/3DOM-Al$_2$O$_3$, (f) Pt@NiO$_x$/3DOM-Al$_2$O$_3$, (g) Pt@CuO$_x$/3DOM-Al$_2$O$_3$.

corresponding to Pt nanoparticles obviously decrease, indicating that TMO nanoparticles cover the surface of Pt nanoparticles, which is an indirect proof of existence of Pt@TMO core-shell nanoparticles. However, the characteristic diffraction peak of TMO was not observed, indicating that TMO nanoparticles with small sizes are highly dispersed on the surface of Pt/3DOM-Al$_2$O$_3$ catalyst. The average crystallite size (D) of 3DOM-Al$_2$O$_3$ calculated by the Debye-Scherrer equation using the half-height width of (440) crystal plane peak is 13.8 nm, as shown in Table 1. Pt@TMO/3DOM-Al$_2$O$_3$ catalysts exhibited the similar XRD patterns, indicating that the morphology of TMO nanoparticles on the surface of Pt/3DOM-Al$_2$O$_3$ catalyst is similar. All in all, it can be concluded that the introduction of TMO nanoparticles on the surface of Pt/3DOM-Al$_2$O$_3$ catalyst can form core-shell structured Pt@TMO nanoparticles which have negligible impact on the nature of 3DOM Al$_2$O$_3$ support, such as crystalline phase, crystalline size and crystallinity.

N$_2$ adsorption-desorption experiments were carried out to examine the porous characteristics of all samples. N$_2$ adsorption-desorption isotherms and pore size distributions using the BJH method of Pt@TMO/3DOM-Al$_2$O$_3$ catalysts are shown in Figure S7. As shown in Figure S7A, all materials clearly display that a nearly linear correlation between absorbed volume and relative pressure is observed in the relative pressure (P/P$_0$) range from 0 to 0.4, which could be ascribed to unrestricted monolayer-multilayer adsorption, suggests that the materials were macroporous adsorbents [43]. The N$_2$ adsorption-desorption

isotherms exhibited a typical IV isotherm with an H2 hysteresis loop in the relative pressure (P/P$_0$) range of 0.4-0.8, which is related to the capillary condensation taking place in mesopores, indicates the existence of mesopores in the skeletons of 3DOM Al$_2$O$_3$. That is to say, a bimodal (macro/meso-) porous structure is presented in all the catalysts. Furthermore, a type IV N$_2$ adsorption-desorption isotherms with a type H3 hysteresis loop, indicating a capillary condensation associated with macropores in the catalysts, is presented in the relative pressure (P/P$_0$) range from 0.8 to 1.0 in the IUPAC classification. It indicates that Pt@TMO/3DOM-Al$_2$O$_3$ catalysts do not clearly exhibit any adsorption saturation at the relative pressure (P/P$_0$) close to unity, which is usually connected with the presence of macropores.

BET surface area (S$_{BET}$) and total pore volume (V$_P$) of the catalysts determined from isotherms are listed in Table 1. BET surface areas of all the catalysts are in the range of 41-60 m^2 g^{-1}, which is mainly caused by the intergranular pore, and no significant difference exists in the BET surface areas among Pt@TMO/3DOM-Al$_2$O$_3$ catalysts. The total pore volumes of all the catalysts were in the ranges of 0.11-0.17 cm^3 g^{-1}. Based on the results of BJH pore size distribution curves derived from the desorption branch of N$_2$ adsorption-desorption isotherms in Figure S7B, average mesopore sizes of the catalysts were evaluated in the range of 3–12 nm. The result further indicates that 3DOM structured materials possess the intergranular mesopores.

3.3. H$_2$-TPR profiles

H$_2$-TPR measurement is a widely applied technology for determining the reducibility of a metallic ion that has potential to remove or take up an oxygen species, which is directly correlated to catalytic performance in a deep oxidation reaction. Fig. 3 shows the H$_2$-TPR profiles of Pt@TMO/3DOM-Al$_2$O$_3$ catalysts. For 3DOM Al$_2$O$_3$, hydrogen consumption is not observed at the region of 100–800 °C, indicating that Al$_2$O$_3$ is inactive in deep oxidation reaction. After introduction of Pt nanoparticles, a weak reduction peak appears at 70 °C in the range of 30–500 °C, which is assigned to the reduction of Pt$^{&+}$ species on the surface of supported Pt NPs, suggesting the relatively low redox capability of Pt/3DOM-Al$_2$O$_3$, provides an ideal condition to investigate the interface effect of supported Pt@TMO core-shell nanoparticles. After further introduction of TMOs shell deposition on the surface of supported Pt nanoparticles (core), Pt@TMOs/3DOM-Al$_2$O$_3$ catalysts show three apparent reduction peaks centered at ∼80, ∼250 and ∼500 °C, except Pt@MnO$_x$/3DOM-Al$_2$O$_3$ catalyst. The reduction peaks located at 80 °C are related to reduction of Pt$^{&+}$ species on the surface of catalysts. The other reduction peaks are assigned to the stepwise reduction of adsorbed oxygen species and Pt@TMO core-shell nanoparticles [44].

In the H$_2$-TPR profile of Pt@FeO$_x$/3DOM-Al$_2$O$_3$ catalyst, H$_2$ consumption peak located at 264 °C is assigned to reduction of bulk Fe$_2$O$_3$

Table 1
BET surface areas, pore volumes, macropore diameters, mesopore diameters, average crystallite sizes and average particle sizes of the Pt@TMO/3DOM-Al$_2$O$_3$ catalysts.

Sample	Macropore Diameter[a] (nm)	Mesopore diameter[b] (nm)	S$_{BET}$ (m^2/g)	Vp (cm^3/g)	Pt size[c] (nm)	Al$_2$O$_3$ size[d] (nm)	Pt actual amounts[e] (wt %)
3DOM Al$_2$O$_3$	290-320	3-9	41.2	0.11	–	13.8	–
Pt/Al$_2$O$_3$	280-320	4-12	50.4	0.13	4.9	13.8	3.8
Pt@MnO$_x$/Al$_2$O$_3$	270-310	3-10	55.6	0.15	5.0	13.5	3.7
Pt@FeO$_x$/Al$_2$O$_3$	280-300	4-9	60.0	0.17	4.8	12.9	3.6
Pt@CoO$_x$/Al$_2$O$_3$	290-310	3-11	56.4	0.14	4.8	14.1	3.7
Pt@NiO$_x$/Al$_2$O$_3$	280-320	4-10	56.5	0.16	4.9	13.8	3.6
Pt@CuO$_x$/Al$_2$O$_3$	290-320	3-11	53.9	0.15	4.6	13.6	3.7

[a] Determined by the SEM images.
[b] Determined by the BJH pore size distributions.
[c] Determined by the TEM images.
[d] Determined by XRD.
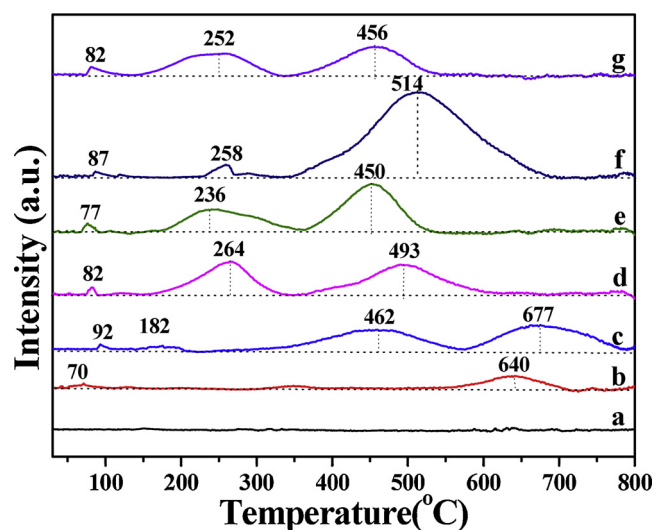[e] Determined by ICP-OES.

Fig. 3. The H₂-TPR profiles of 3DOM Al₂O₃, Pt/3DOM-Al₂O₃ and Pt@TMO/3DOM-Al₂O₃ catalysts. (a) 3DOM-Al₂O₃; (b) Pt/3DOM-Al₂O₃; (c) Pt@MnOₓ/3DOM-Al₂O₃; (d) Pt@FeOₓ/3DOM-Al₂O₃; (e) Pt@CoOₓ/3DOM-Al₂O₃; (f) Pt@NiOₓ/3DOM-Al₂O₃; (g) Pt@CuOₓ/3DOM-Al₂O₃.

to Fe₃O₄, while the reduction peak appeared at 493 °C is assigned to the reduction transformation of Fe₃O₄ to FeO (600 °C for reduction of general Fe₃O₄ to FeO) [45]. For Pt@NiOₓ/3DOM-Al₂O₃ catalyst, the first reduction peaks at 258 °C is due to the reduction of surface oxygen species, and the other reduction peaks at a relatively higher temperature (514 °C) is assigned to the reduction of Pt-NiAlOₓ, which is located at 790 °C for the reduction of NiAl₂O₄ [46]. For Pt@CuOₓ/3DOM-Al₂O₃ catalyst, the reduction peaks at 252 and 456 °C can be attributed to the stepwise reduction of Cu²⁺ to Cu⁺ (283 °C for pure CuO) and Cu⁺ to Cu°, respectively[47]. The Pt@CoOₓ/3DOM-Al₂O₃ catalyst shows the strong reduction peak centered at 236 °C and 450 °C, which are ascribed to the reduction of Co³⁺→Co²⁺ (492 °C for pure Co₃O₄) and Co²⁺→Co° (540 °C for pure CoO), respectively [48]. For the Pt@MnOₓ/3DOM-Al₂O₃ catalyst, the weak reduction peak at 182 °C is assigned to the reduction of the surface oxygen species, and the strong reduction peaks at ~462 °C and ~677 °C are assigned to the reduction of Mn⁴⁺ to Mn³⁺ (404 °C for MnO₂) and Mn³⁺ to Mn²⁺ (608 °C for Mn₃O₄), respectively [49]. It is worth noting that the reduction peaks of Pt@TMO/3DOM-Al₂O₃ catalysts are apparently shifted to the lower temperature after introduction of transition metal oxides covered supported Pt nanoparticles, especially Pt@CoOₓ/3DOM-Al₂O₃ catalyst. It indicates that the redox ability of Pt-based catalysts can be improved, which is contributed to the strong interaction between Pt and TMOs in supported Pt@TMO core-shell nanoparticles observed from TEM images. The formation of Pt-O-M bonds at interface of Pt-TMO can improve reducibility of core-shell nanostructured Pt@TMO nanoparticles, and even resulting in spillover of atomic hydrogen from Pt to oxide surface occurs more easily [50]. Thus, the strong interaction between Pt nanoparticles and transition metal oxides gives rise to an improvement in the low-temperature reducibility of Pt@TMO/3DOM-Al₂O₃ catalysts, which would be beneficial for enhancement in catalytic performance during soot oxidation.

3.4. XPS spectra

The densities of active sites and active oxygen species on the surface of Pt@TMO/3DOM-Al₂O₃ catalysts are related to surface state of supported Pt@TMO core-shell nanoparticles. Since the Pt 4f line was overlapped with the strong Al 2p peak of Al₂O₃ support in the region around 70.0–80.0 eV, the valence of Pt can only be obtained from the Pt 4d line. Fig. 4 shows XPS of Pt4d and O1s regions over Pt@TMO/
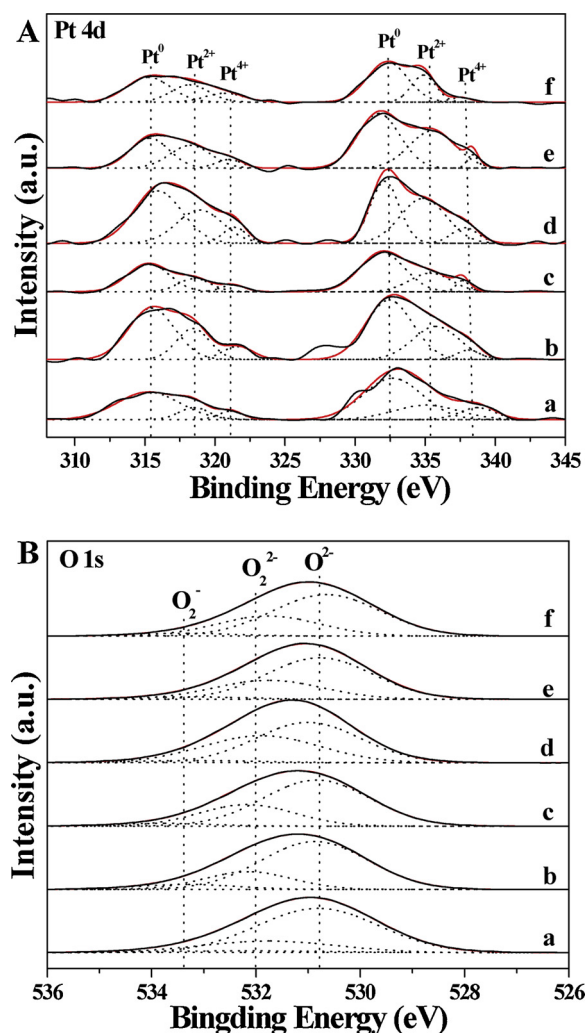

Fig. 4. X-ray photoelectron spectra (XPS) of (A) Pt4d and (B) O1s regions for Pt/3DOM-Al₂O₃ and Pt@TMO/3DOM-Al₂O₃ catalysts. (a) Pt/3DOM-Al₂O₃; (b) Pt@MnOₓ/3DOM-Al₂O₃; (c) Pt@FeOₓ/3DOM-Al₂O₃; (d) Pt@CoOₓ/3DOM-Al₂O₃; (e) Pt@NiOₓ/3DOM-Al₂O₃; (f) Pt@CuOₓ/3DOM-Al₂O₃.

3DOM-Al₂O₃ catalysts. As shown in Fig. 4(A), Pt4d XPS can be deconvoluted into three lines using the standard procedure. The pairs of binding energies centered at 315.5 and 332.6 eV, 318.4 and 335.8 eV, and 321.6 and 338.1 eV are assigned to Pt°, Pt²⁺ and Pt⁴⁺ species, respectively, indicating that both metallic (majority) and ionic Pt species coexist in Pt/3DOM-Al₂O₃ and Pt@TMO/3DOM-Al₂O₃ catalysts. It is well known that ionic Pt species, induced by the strong Pt-TMO interaction, is active site for adsorption and activation of O₂ and NO. Therefore, these deconvolution results allow us to estimate the relative amount of each Pt species on Pt@TMO/3DOM-Al₂O₃ catalysts, and the results are shown in Table 2. Pt species ratio (Rᵃ) of Pt⁺(Pt²⁺ and Pt⁴⁺) to Pt° over Pt/3DOM-Al₂O₃ catalyst is only 0.458. After introduction of TMO shell, the Rᵃ values of catalysts increase obviously due to the strong Pt-TMO interaction at the interface of Pt@TMO core-shell nanostructure, which results in increasing the density of active oxygen species for soot oxidation [51]. In addition, the relative ratios of Pt⁺ species in Pt@TMO/3DOM-Al₂O₃ catalysts are obviously different in Table 2. It suggests that there is a discriminatory intensity of the strong Pt(core)-TMO(shell) interaction, which results in the surface density of Pt⁺ species due to the electron transfer from Pt° to M⁺ at the core-shell interface. Further, the local lattice structure distortion of state transition metal atoms located at interface of Pt@TMO core-shell nanoparticles would give rise to the migration of lattice oxygen from

Table 2
Surface compositions and oxidation states of Pt and O species over Pt@TMO/3DOM-Al$_2$O$_3$ catalysts derived from XPS analyses.

sample (3DOM)	Pt species				O species			
	Pt°/%	Pt^{2+}/%	Pt^{4+}/%	R^a	O$_2^-$/%	O$_2^{2-}$/%	O^{2-}/%	R^b
Pt/Al$_2$O$_3$	68.6	21.3	10.1	0.458	5.2	21.6	73.2	0.366
Pt@MnO$_x$/Al$_2$O$_3$	61.8	30.7	7.5	0.618	3.6	28.2	68.2	0.466
Pt@FeO$_x$/Al$_2$O$_3$	66.3	27.0	6.7	0.508	7.0	21.7	71.3	0.403
Pt@CoO$_x$/Al$_2$O$_3$	49.8	41.2	9.0	1.008	3.6	41.3	55.1	0.815
Pt@NiO$_x$/Al$_2$O$_3$	53.3	41.0	5.7	0.876	4.4	30.5	65.1	0.536
Pt@CuO$_x$/Al$_2$O$_3$	61.0	29.3	9.7	0.639	3.9	30.3	65.8	0.520

[a] The Pt species ratio of the Pt$^{\&+}$ (Pt^{2+} + Pt^{4+}) to Pt°.
[b] Determined by the oxygen species ratio of the adsorbed oxygen (O$_2^-$ + O$_2^{2-}$) to lattice oxygen (O^{2-}).

TMO shell to the interface of Pt-TMO and maintain Pt species at the high-valent state [36]. Among prepared catalysts, Pt@CoO$_x$/3DOM-Al$_2$O$_3$ catalyst shows the largest R^a value (1.008) in Table 2, while the R^a value of Pt@FeO$_x$/3DOM-Al$_2$O$_3$ catalyst is only 0.508. This result indicates that the density of surface Pt$^{\&+}$ species depends on the strong interaction between Pt core and TMO shell, and Pt(core)-CoO$_x$(shell) nanoparticles show the optimal interaction for increasing the density of active sites for O$_2$ and NO activation, which is in accordance with the results of H$_2$-TPR.

To investigate surface-active oxygen species, O1s XPS spectra of Pt@TMO/3DOM-Al$_2$O$_3$ catalysts are shown in Fig. 4(B). The asymmetrical O1s spectrum was decomposed into three surface species: lattice oxygen (O^{2-}) species at 530.8 eV, peroxide (O$_2^{2-}$) species at 532.0 eV and superoxide (O$_2$-) species at 533.4 eV. The ratio (R^b) values of active oxygen species (O$_2$- and O$_2^{2-}$) to O^{2-} over Pt@TMO/3DOM-Al$_2$O$_3$ catalysts are remarkably larger than those of the Pt/3DOM-Al$_2$O$_3$ catalyst, as shown in Table 2. This result suggests that Pt@TMO core-shell structure can enhance the amount of surface active oxygen species, which may be attributed to the interface effect between Pt core and TMO shell for improving the capability of oxygen activation and promoting lattice oxygen transference from TMO to Pt-TMO interface. It has been reported that the amount of surface O$_2^{2-}$ and O$_2$ species is strongly related to the catalytic activity for soot oxidation [30]. Therefore, Pt@TMO/3DOM-Al$_2$O$_3$ catalysts should show higher catalytic performances for soot oxidation than Pt/3DOM-Al$_2$O$_3$ catalyst. In addition, the R^b values of Pt@TMO/3DOM-Al$_2$O$_3$ catalysts decreased in the order of Pt@Co$_3$O$_4$/3DOM-Al$_2$O$_3$ (0.815) > Pt@NiO/3DOM-Al$_2$O$_3$ (0.536) > Pt@CuO/3DOM-Al$_2$O$_3$ (0.520) > Pt@Mn$_2$O$_3$/3DOM-Al$_2$O$_3$ (0.466) > Pt@Fe$_2$O$_3$/3DOM-Al$_2$O$_3$ (0.403). It suggests that the density of active oxygen species (O$_2^{\&-}$) over Pt@TMO/3DOM-Al$_2$O$_3$ catalysts is strongly correlated with the role of the transition metal oxide shells. Pt@CoO$_x$/3DOM-Al$_2$O$_3$ catalyst shows the largest R^b value (0.815), indicates that the strong Pt-CoO$_x$ interaction is more favorable for the increase of surface-active oxygen species in contrast to other TMO shells, which supports the results of H$_2$-TPR. Thus, the Pt@CoO$_x$/3DOM-Al$_2$O$_3$ catalyst shows higher catalytic activity for soot oxidation than the other Pt@TMO/3DOM-Al$_2$O$_3$ catalysts.

3.5. Catalytic activity and stability for soot oxidation

We carried out soot-temperature programmed oxidation (soot-TPO) tests to investigate catalytic activity of Pt@TMO/3DOM-Al$_2$O$_3$ catalysts for soot oxidation under condition of loose contact between soot and catalysts in the presence of O$_2$ (5%), NO (0.2%) and H$_2$O (5%), and the results are shown in Table 3. For comparison, soot oxidation without a catalyst is included, i.e., its T$_{10}$ and T$_{50}$ values are 485 and 589 °C, respectively, which is higher than the temperature of diesel exhaust (< 400 °C). It indicates that diesel soot particles trapped by DPF cannot be oxidized spontaneously, and the catalyst must be applied during soot elimination. 3DOM Al$_2$O$_3$ support exhibits low catalytic activity for soot oxidation, i.e., its T$_{50}$ value is still 535 °C, which is attributed to the

poor redox property of Al$_2$O$_3$. In other words, 3DOM Al$_2$O$_3$ is good inert support to systematical study on the role of strong Pt-TMOs interaction in supported Pt@TMOs core-shell nanoparticles. 3DOM Al$_2$O$_3$ support only provides a role in enhancing the contact efficiency between solid reactants (soot particles) and catalysts. After the introduction of supported Pt nanoparticles, Pt/3DOM-Al$_2$O$_3$ catalyst exhibited good catalytic activity for soot oxidation in comparison with 3DOM-Al$_2$O$_3$ catalyst, as its T$_{50}$ value decreased to 468 °C, indicates that Pt nanoparticles are very active component for NO$_x$-assisted soot oxidation. After further introduction of a supported TMO shell, the catalytic activities of Pt@TMO/3DOM-Al$_2$O$_3$ catalysts for soot oxidation obviously improve, i.e., their T$_{50}$ values shift from approximately 470 °C (Pt/3DOM-Al$_2$O$_3$) to less than 400 °C (Pt@TMO/3DOM-Al$_2$O$_3$). Compared with the catalytic activities of TMO/3DOM-Al$_2$O$_3$ catalysts in Table S1, supported Pt@TMO core-shell nanoparticles are crucial to enhance catalytic activity for diesel soot oxidation, which is related to the strong Pt-TMO interaction. Among the catalysts, Pt@CoO$_x$/3DOM-Al$_2$O$_3$ catalyst exhibits the highest catalytic activity for soot oxidation, i.e., its T_{10}, T_{50}, and T_{90} values are 298, 357 and 397 °C, respectively, which is far lower than those of Pt@CoO$_x$/Al$_2$O$_3$ catalyst without 3DOM structure. Hence, the strong Pt(core)-CoO$_x$(shell) interactions might be used to enhance adsorption-activation properties of O$_2$ and NO reactants. In addition, after introduction of the Pt@TMO core-shell nanoparticles on the surface of 3DOM-Al$_2$O$_3$, the selectivity to CO$_2$ product ($S_{CO_2}^m$) values are remarkably increased to 98%, suggesting that CO emitted from a diesel engine can be immediately oxidized and purified in a practical application. It is probably attributed to Pt@TMO core-shell nanoparticles with the strong oxidation for CO molecule. In other words, the composition and structure of TMO shell and the interface effect between Pt core and TMO shell can strongly influence catalytic activity of Pt@TMO/3DOM-Al$_2$O$_3$ catalysts for soot oxidation.

The apparent TOF values can reflect the activity of Pt@TMO/3DOM-Al$_2$O$_3$ catalysts for soot oxidation. Based on the results of TEM images, ICP-OES and XPS, the actual amounts of Pt$^{\&+}$ species in Pt@TMO/3DOM-Al$_2$O$_3$ catalysts can be used as active site amounts because of the similar particle sizes of Pt@TMO core-shell nanoparticles. To obtain the reaction rates (R) for soot oxidation, an isothermal oxidation reaction at 300 °C was carried out in the kinetic regime. Fig. 5A shows soot conversion amount as a function of time (min) over 3DOM Al$_2$O$_3$, Pt/3DOM-Al$_2$O$_3$ and Pt@TMO/3DOM-Al$_2$O$_3$ catalysts, and the slopes of soot conversion lines are R value (the production of CO$_2$ per unit time) for each catalyst for soot oxidation shown in Table 3. As shown in Fig. 5A, the slopes of 3DOM-Al$_2$O$_3$ and Pt/3DOM-Al$_2$O$_3$ catalysts are much lower than those of Pt@TMO/3DOM-Al$_2$O$_3$ catalysts, indicating that Pt@TMO core-shell nanoparticles can improve the catalytic activity for soot oxidation, and the active sites are located at the interface between Pt core and TMO shell. Among the catalysts, the R value of Pt@CoO$_x$/3DOM-Al$_2$O$_3$ catalyst (15.8 μmol g^{-1} min^{-1}) is the largest. As shown in Table 3, the TOF values of Pt@TMO/3DOM-Al$_2$O$_3$ catalysts are larger than those of the Pt/3DOM-Al$_2$O$_3$, indicating that Pt@TMO core-shell nanoparticles are very active in soot oxidation.

Table 3
Catalytic activity, selectivity, Pt actual amounts, reaction rate (R), apparent activation energy (E_a) and TOF values of 3DOM Al_2O_3, Pt/3DOM-Al_2O_3 and Pt@TMO/3DOM-Al_2O_3 catalysts for soot combustion under loose contact between soot and catalysts.

Catalysts (3DOM)	T_{10} (°C) [a]	T_{50} (°C) [a]	T_{90} (°C) [a]	S_{CO2}^m (%)[a]	R (μmol g^{-1} min^{-1}) [b]	Pt$^{\&+}$ species (μmol) [c]	TOF$_{Pt}$ (10^{-3} s^{-1})	E_a (kJ mol^{-1})[a]
Pure soot	485	589	647	51.2	–			–
Al_2O_3	366	535	588	54.5	0.8	–	–	–
Pt/Al_2O_3	365	468	549	92.0	3.7	6.1	1.01	98
Pt@MnO$_x$/Al_2O_3	309	389	455	98.2	8.9	7.3	2.04	71
Pt@FeO$_x$/Al_2O_3	313	398	466	98.1	7.6	6.2	2.03	76
Pt@CoO$_x$/Al_2O_3	298	357	397	98.2	15.8	9.5	2.76	52
Pt@NiO$_x$/Al_2O_3	303	363	403	98.2	13.1	8.6	2.53	61
Pt@CuO$_x$/Al_2O_3	317	379	416	98.3	10.8	7.4	2.43	67
Pt@CoO$_x$/Al_2O_3[d]	316	396	433	99.1	–	–	–	–

[a] Reaction condition: 5% O_2, 0.2% NO and 5% H_2O in Ar, 50 ml min^{-1}.
[b] Reaction gas, 5% O_2, 0.2% NO and 5% H_2O in Ar, 50 ml min^{-1} at 300 °C.
[c] Determined by the results of XPS and ICP-OES.
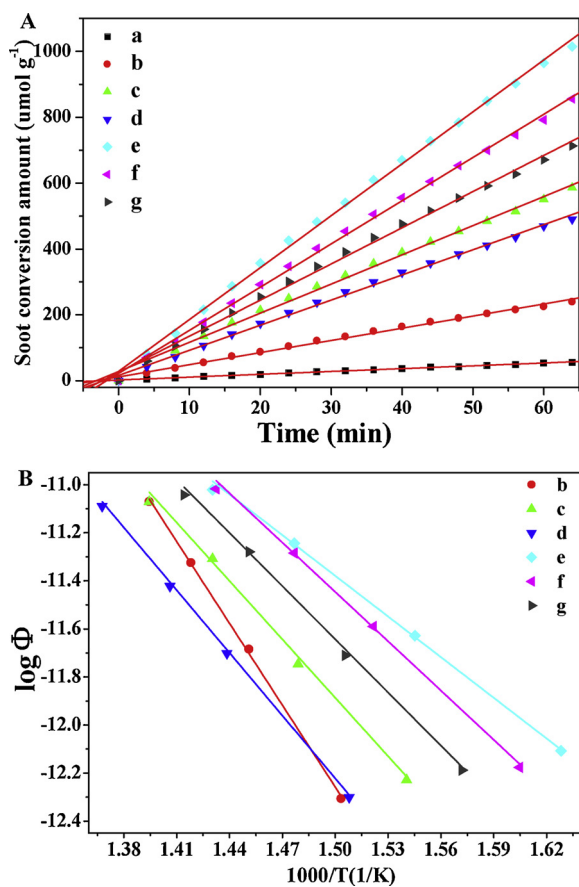[d] Reference catalyst without macropores.

Fig. 5. The rates of soot conversion at 300 °C (A) and the Ozawa plots (B) for soot conversion of 50% with varying increasing temperature rates of 2, 4, 6 and 10 °C min^{-1} under conditions of in the presence of O_2 (5%), NO (0.2%) and H_2O (5%). (a) 3DOM-Al_2O_3; (b) Pt/3DOM-Al_2O_3; (c) Pt@MnO$_x$/3DOM-Al_2O_3; (d) Pt@FeO$_x$/3DOM-Al_2O_3; (e) Pt@CoO$_x$/3DOM-Al_2O_3; (f) Pt@NiO$_x$/3DOM-Al_2O_3; (g) Pt@CuO$_x$/3DOM-Al_2O_3.

Pt@CoO$_x$/3DOM-Al_2O_3 catalyst shows the highest activity with the largest TOF value (2.76×10^{-3} S^{-1}), which is approximately 2.5 times that of Pt/3DOM-Al_2O_3 catalyst (1.01×10^{-3} S^{-1}) at 300 °C, indicating that the catalytic activity of Pt@TMO/3DOM-Al_2O_3 catalysts for soot oxidation is dependent on the strong Pt-TMO interaction, which is in accordance with the soot-TPO results.

The apparent activation energy (E_a) of the catalysts is also an important index to evaluate the reaction kinetics. Fig. 5B and Table 3 show the Ozawa plots and the E_a values of Pt/3DOM-Al_2O_3 and

Pt@TMO/3DOM-Al_2O_3 catalysts for 50% soot conversion, with varying rising temperature rates of 2 °C, 4 °C, 6 °C and 10 °C min^{-1}. The E_a value of Pt/3DOM-Al_2O_3 catalyst is 98 kJ mol^{-1}. After the introduction of TMO shell, the E_a values decrease obviously to 52–76 kJ mol^{-1}, suggesting that Pt@TMO/3DOM-Al_2O_3 catalysts for soot oxidation have lower energy barriers in comparison to Pt/3DOM-Al_2O_3 catalyst. It indicates that Pt@TMO core-shell nanoparticles can improve the catalytic activity of soot oxidation. Among the catalysts, the E_a value of Pt@CoO$_x$/3DOM-Al_2O_3 catalyst (52 kJ mol^{-1}) is the lowest, which is in accord with its largest reaction rate for catalytic soot oxidation.

To observe the catalytic stability of Pt@TMO/3DOM-Al_2O_3 catalysts for soot oxidation in the presence of O_2 (5%), NO (0.2%) and H_2O (5%), the catalytic activity and selectivity of a typical Pt@CoO$_x$/3DOM-Al_2O_3 catalyst during four soot-TPO cycles are shown in Fig. 6. The values of T_{10}, T_{50} and T_{90} do not change significantly. Meanwhile, Pt@CoO$_x$/3DOM-Al_2O_3 catalyst maintains high S_{CO2}^m during four cycles of soot-TPO tests, i.e., the numerical values of S_{CO2}^m are ~99%. In addition, Figure S8 shows TEM and HRTEM images of Pt@CoO$_x$/3DOM-Al_2O_3 catalyst after four cycles of soot-TPO tests. The nanostructures of 3DOM and Pt@CoO$_x$ core-shell are not changed, indicating that the catalysts of 3DOM-Al_2O_3 supported Pt@TMO core-shell nanoparticles with the strong Pt-TMO interaction have both good structure stability and good catalytic stability during soot oxidation.

The performances of catalysts during soot oxidation are influenced by vehicle emissions (NO, H_2O and SO_2) in practical application, thus, a catalyst needs to excellent H_2O and SO_2 resistances. To investigate the effect of SO_2 and H_2O on catalytic activity for soot oxidation, Fig. 7 shows catalytic activities (T_{10}, T_{50}, T_{90} and S_{CO2}^m values) of Pt@TMO/
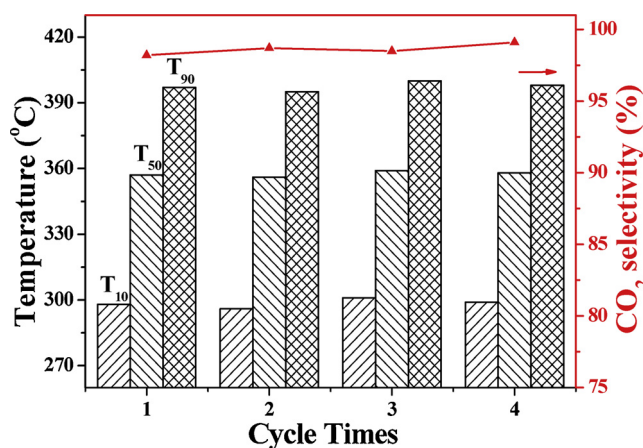

Fig. 6. Stability test and CO_2 selectivity of the Pt@CoO$_x$/3DOM-Al_2O_3 catalyst for soot combustion in the presence of O_2(5%), NO(0.2%) and H_2O(5%).
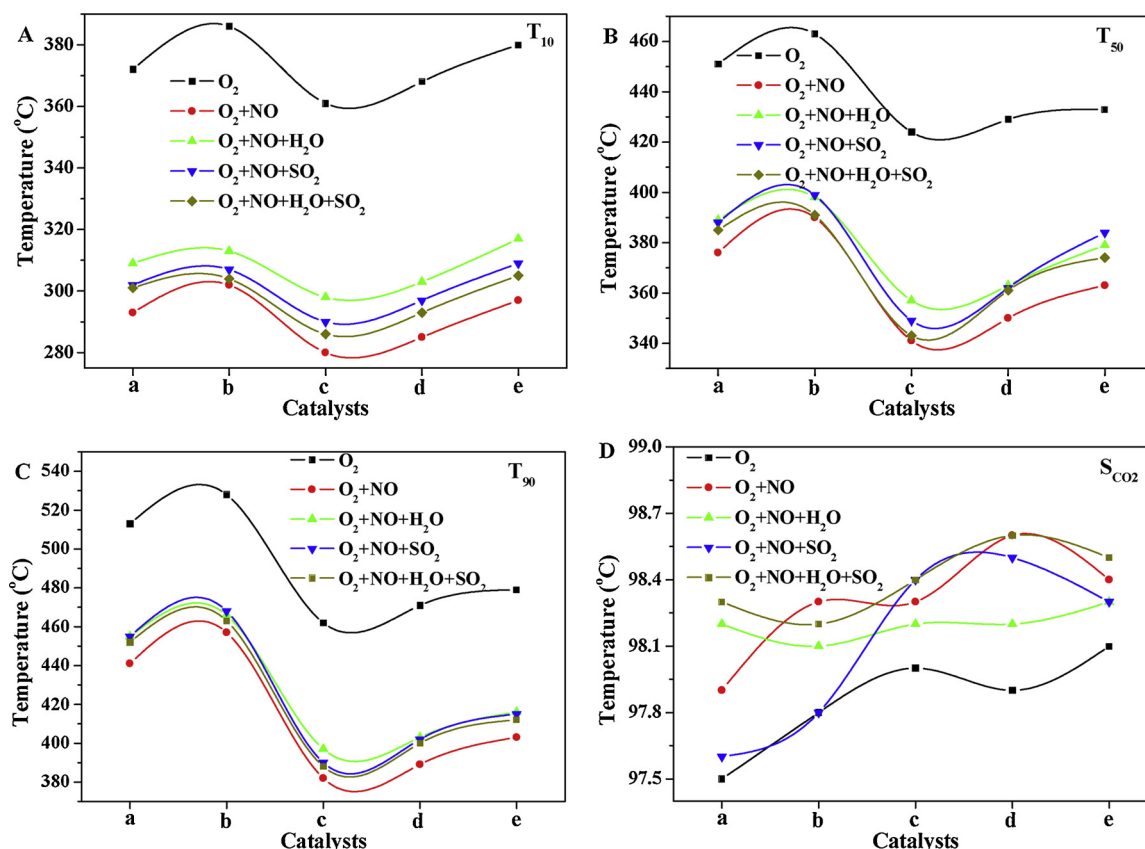
Fig. 7. The T_{10} (A), T_{50} (B), T_{90} (c) and $S_{CO_2}^{m}$ (D) values of Pt@TMO/3DOM-Al_2O_3 catalysts for soot oxidation under conditions of O_2(5%), O_2(5%) + NO(0.2%), O_2(5%) + NO(0.2%) + H_2O(5%), O_2(5%) + NO(0.2%) + SO_2(0.02%), O_2(5%) + NO(0.2%) + H_2O (5%) + SO_2(0.02%). (a) Pt@MnO_x/3DOM-Al_2O_3; (b) Pt@FeO_x/3DOM-Al_2O_3; (c) Pt@CoO_x/3DOM-Al_2O_3; (d) Pt@NiO_x/3DOM-Al_2O_3; (e) Pt@CuO_x/3DOM-Al_2O_3.

3DOM-Al_2O_3 catalysts for soot oxidation under conditions of in the presence or absence of NO (0.2%), H_2O (5%) and SO_2 (0.02%). It is noted that the role of NO gas is crucial to enhance catalytic activity for soot oxidation. For instance, after introduction of NO gas, the T_{50} values of Pt@TMO/3DOM-Al_2O_3 catalysts decrease more than 70 °C in comparison to those of in the presence of only O_2 gas. For in the presence of NO (0.2%) and H_2O (5%), the catalytic activities of Pt@TMO/3DOM-Al_2O_3 catalysts for soot oxidation decrease obviously, especially the T_{10} value. The inhibiting effect of H_2O on catalytic activity may be attributed to the coverage of H_2O on the surface of active sites during soot oxidation at relatively low temperature. For in the presence of NO (0.2%) and SO_2 (0.02%), the catalytic activities of Pt@TMO/3DOM-Al_2O_3 catalysts for soot oxidation decrease slightly, indicating that the catalysts have good SO_2 tolerance performance, which may be related to the surface acidity of 3DOM-Al_2O_3 support for inhibition of SO_2 adsorption. After the introduction of both H_2O (5%) and SO_2 (0.02%), the catalytic activities of Pt@TMO/3DOM-Al_2O_3 catalysts for soot oxidation increase slightly instead of decreasing in comparison to those of in the single presence of H_2O (5%) or SO_2 (0.02%), and even the T_{50} value (343 °C) of Pt@CoO_x/3DOM-Al_2O_3 catalyst is lower than that of none of H_2O and SO_2, which is accord with the results reported by Uchisawa [52]. In addition, Pt@TMO/3DOM-Al_2O_3 catalysts still show high the selectivity of CO_2 product after introduction of H_2O (5%) and SO_2 (0.02%), i.e., the $S_{CO_2}^{m}$ values are always larger than 97.5%. It indicates that the selectivity of CO_2 product for soot oxidation is not influenced by H_2O and SO_2. From the above, Pt@TMO/3DOM-Al_2O_3 catalysts have excellent H_2O and SO_2 resistances and even the enhancing effect during catalytic soot oxidation. Therefore, Pt@TMO/3DOM-Al_2O_3 catalysts are promising to practical application of emission reduction of diesel soot.

4. Discussion

4.1. The migration path of active oxygen species in catalytic soot oxidation

It is generally known that the catalytic oxidation of diesel soot is a complicated heterogeneous catalytic process involving three phases of solid catalyst, solid soot and gas reactants (O_2, NO). The migration of active oxygen (O_a) species from catalyst to soot is an important factor for soot oxidation, which consists of direct (catalyst-O_a-soot) and indirect (catalyst-O_a-NO-NO_2-soot) pathways [53]. In the direct pathway, the good contact efficiency between catalyst and soot is extremely beneficial to active oxygen species transfer process. And the catalytic activity of soot oxidation in loose contact is more important than those in tight contact owing to the fact of loose contact between catalyst and soot particle under practical engine operation conditions. The structure and physicochemical states of a catalyst can affect its catalytic performance for soot oxidation. In many studies, generally catalysts have small pore sizes or no pores, and its external surfaces are only available for soot oxidation because their pore diameters (< 10 nm) are much smaller than the diameter of soot particles (> 25 nm). It is necessary to design and prepare a catalyst which enhances the contact area between catalyst and soot under loose contact conditions. 3DOM materials with periodic big pore sizes are designed and synthesized by a PMMA colloidal crystal template method. In our previous works, it was proved that 3DOM structure can dramatically enhance contact efficiency between active sites and soot particles because of permit of soot into the interior pores, which is beneficial for the migration of active oxygen species from catalyst to soot whatever direct and indirect pathways [50]. Thus, 3DOM material is a desirable structure for catalytic soot oxidation.

In order to verify the migration path of active oxygen species in

catalytic soot oxidation, the effect of NO on catalytic activity for soot oxidation was investigated. Fig. 7 shows the catalytic activities of Pt/3DOM-Al$_2$O$_3$ and Pt@TMO/3DOM-Al$_2$O$_3$ catalysts for soot oxidation in the presence or absence of NO. It is worth noting that the activities of catalytic soot oxidation in presence of NO increased obviously in comparison with those of in the absence of NO, indicating that the role of NO is very important to promote the catalytic activity for soot oxidation. In other words, the indirect NO$_2$-assisted mechanism is the dominant pathway for soot oxidation because NO$_2$ acts as an efficient mobile oxidizing agent, although 3DOM structure can weaken the dependence of catalytic activity on NO$_2$ intermediate [54]. Thus, the active oxygen species at the Pt-TMO interface can migrate to the surface of diesel soot particles by using NO$_2$ as an intermediate oxidant which can oxidize soot to CO$_2$, i.e., the indirect pathway (NO + 1/2O$_2$→NO$_2$ and NO$_2$ + soot→CO$_2$). Finally, the catalytic NO oxidation to NO$_2$ is the rate-determining factor for soot oxidation.

4.2. The effect of strong Pt-TMO interaction on catalytic soot oxidation

The reaction nature of catalytic soot oxidation is complex deep oxidation process. The oxidation capability of active sites is strongly dependent on the Pt-TMO interaction, which is the property in improving catalytic activity for soot oxidation. In other words, the redox property of Pt@TMO/3DOM-Al$_2$O$_3$ catalysts with strong core-shell interaction is strongly related to the catalytic performances of themselves. Based on the results of H$_2$-TPR in Fig. 3, Pt@TMO/3DOM-Al$_2$O$_3$ catalysts show strong reduction peaks at lower temperature in comparison with 3DOM-Al$_2$O$_3$ and Pt/3DOM-Al$_2$O$_3$ catalysts. Low temperatures and large reduction peak areas can reflect the good reducibility. Combined with soot-TPO results in Table 3, the catalytic activities for soot oxidation have good correlation with H$_2$ consumption (peak area) at low temperature, indicating that the catalytic activity is strongly dependent on the properties of TMO shell originating from the strong Pt (core)-TMO(shell) interaction. The coordination unsaturated metal cations located at the interface of Pt-TMO can promote adsorption-activation of O$_2$ and can deliver oxygen species migration from lattice to surface of the catalyst, which improves reducibility of supported Pt@TMO core-shell nanoparticles. Among the catalysts, Pt@CoO$_x$/3DOM-Al$_2$O$_3$ catalyst with strong redox property shows the optimal interface interaction to improve catalytic activity for soot oxidation.

The rate-determining factor of catalytic NO oxidation to NO$_2$ for soot oxidation was further investigated by NO-TPO. Fig. 8 shows NO$_2$ concentration derived from NO oxidized over Pt@TMO/3DOM-Al$_2$O$_3$ catalysts detected by MS. For comparison, NO$_2$ concentration profiles

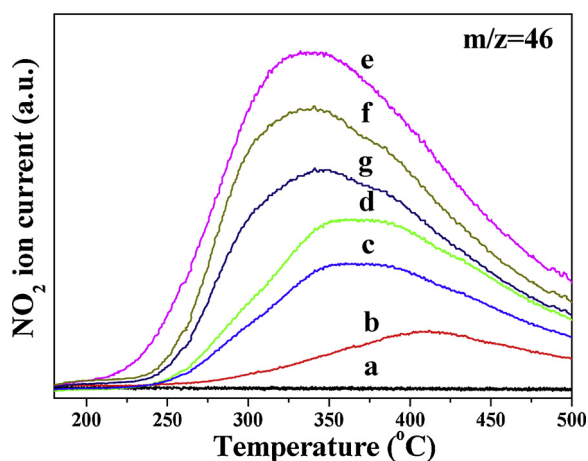**Fig. 8.** The outlet NO$_2$ ion current curves during NO oxidation process detected by mass spectrometry. (a) Without catalyst, (b) Pt/3DOM-Al$_2$O$_3$, (c) Pt@MnO$_x$/3DOM-Al$_2$O$_3$, (d) Pt@FeO$_x$/3DOM-Al$_2$O$_3$, (e) Pt@CoO$_x$/3DOM-Al$_2$O$_3$, (f) Pt@NiO$_x$/3DOM-Al$_2$O$_3$, (g) Pt@CuO$_x$/3DOM-Al$_2$O$_3$.

without a catalyst and over Pt/3DOM-Al$_2$O$_3$ catalyst are also included. NO$_2$ was not detected in the case of without catalyst below 500 °C, while NO$_2$ peak of Pt/3DOM-Al$_2$O$_3$ catalyst is clearly observed. NO$_2$ concentration cannot increase with temperature rising until the thermodynamic equilibrium of the equation (NO + 1/2O$_2$⟷NO$_2$), and then decreases at higher temperatures. After introduction of TMO shell, NO$_2$ concentrations of Pt@TMO/3DOM-Al$_2$O$_3$ catalysts remarkably increased due to the interfacial effect of Pt-TMO on promoting the efficiency of NO oxidation. Pt@CoO$_x$/3DOM-Al$_2$O$_3$ catalyst, in particular, shows the largest NO$_2$ concentration peak, indicating that the strong Pt-CoO$_x$ interaction is favorable for improving the catalytic activity for NO oxidation, which is in accord with the results of soot-TPO and can explain the high catalytic activity of Pt@TMO core-shell catalyst for soot oxidation in the presence of NO.

4.3. DFT calculations for NO oxidation

It is well known that the oxygen vacancies or coordinatively unsaturated metal cations located at the metal-oxide interfaces are active sites for promoting the adsorption-activation of O$_2$ and NO in soot oxidation reaction. Based on the experimental observations of XPS measurements (Fig. 4), the active oxygen species over Pt@TMO/3DOM-Al$_2$O$_3$ catalysts are mainly derived from the core-shell interfaces, and the core-shell boundaries serve as a reservoir for oxygen species in soot oxidation. It is concluded that the catalytic performances of catalysts depend on the density of metal-oxide interface active sites. Therefore, design and preparation of active sites with a high density on the surface of 3DOM-Al$_2$O$_3$ is critical for enhancing the catalytic activity of soot oxidation. The density of active sites can be improved by fabrication of core-shell structured Pt@TMO Nanoparticles as a result of the optimization of the Pt-Al$_2$O$_3$ interface. And, the strong interaction between Pt core and TMO shell, which increases the concentration of active oxygen species. Pt@TMO/3DOM-Al$_2$O$_3$ catalysts with high density of active sites will show higher TOF and lower E_a values in comparison with ordinary Pt/3DOM-Al$_2$O$_3$ catalyst (Table 3). It suggests that the catalytic activity of soot oxidation over Pt@TMO/3DOM-Al$_2$O$_3$ catalysts is strongly related to the role of transition metal oxide shell.

To reveal the catalytic mechanism for soot oxidation, DFT calculations for catalytic NO oxidation over supported Pt@TMO core-shell nanoparticles were carried out, and the results are shown in Fig. 9. The reaction pathway for NO oxidation follows the Langmuir-Hinshelwood mechanism, which can be described as: Firstly, NO and O$_2$ adsorb on the surface, and the adsorbed O$_2$* dissociates into atomic O* species. Secondly, adsorbed NO* combines with O* to form adsorbed NO$_2$*, and then NO$_2$ species desorb from the surface of the catalysts. Thirdly, NO adsorbs on the surface again and combines with the other O* to form adsorbed NO$_2$*. Finally, adsorbed NO species were oxidized to NO$_2$ species by the surface active oxygen species. Based on the results of Figures S9 and S10 and Table S2, it is revealed that NO molecules prefer to adsorb and occupy large numbers of active sites on the surface of the bare Pt(111) model, while O$_2$ molecules are strongly adsorbed by the coordination-unsaturated (CUS) cations at the boundaries of TMO/Pt(111) model (Steps I-III). Figure S11 and Table S3 show the optimized structures and dissociation barriers of O$_2$ dissociation at the Pt-TMO interface. The dissociation energy barriers (TS^{-1}) for O−O bond cleavage are lower than that of bare Pt(111) surface (0.88 eV), especially the lowest CoO$_x$/Pt(111) model (0.03 eV). The dissociated oxygen atoms coordinate with exposed CUS cations (Step IV). The adsorbed NO molecule and dissociated atomic O can combine to form NO$_2$ (Step V, Figure S12). The calculated energy barriers (TS^{-2}) of first NO$_2$ formation on Pt-TMO (Mn, Fe, Co, Ni, Cu) models are 1.34, 1.17, 1.22, 0.85 and 0.63 eV, respectively, as shown in Table S4, and are lower than that on the Pt(111) surface (1.67 eV). The NO$_2$ desorption, an important pathway for NO oxidation, occurs at the Pt-TMO interface, and the Pt-TMO (Co, Ni, Cu) models show the relatively low energy barriers (Step VI). Consequently, the residual O atom of dissociated O−O bond can
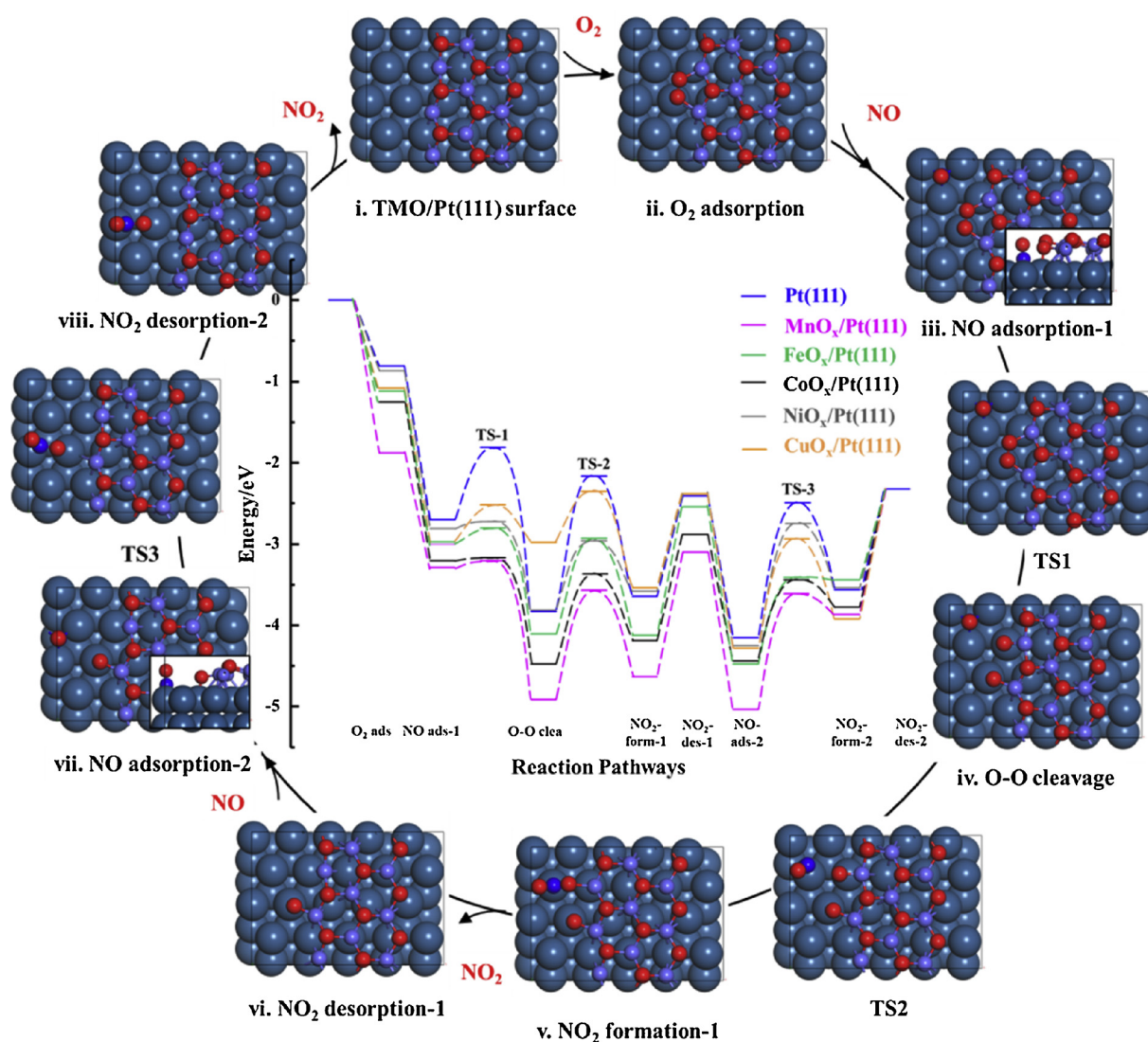
Fig. 9. Reaction pathways for NO oxidation over the Pt@TMO/3DOM-Al$_2$O$_3$ catalysts.

combine with another adsorbed NO molecule to form the second NO$_2$ (Steps VII-VIII, Figure S13) and can finish the overall reaction. CoOx/Pt (111) model exhibits the lowest energy barrier (0.94 eV) for the second NO$_2$ formation (TS^{-3}), as shown in Table S5.

In addition, the micro-kinetic study of the NO oxidation over TMO/Pt(111) models was carried out, and the results are shown in Table 4. For Pt@MnO$_x$, Pt@FeO$_x$ and Pt@CoO$_x$ catalysts, the step of NO$_2$ desorption has the largest degree of rate control (X_{RC}) value at 550 K, suggesting that the step is rate-determining step for NO oxidation over the catalysts. For Pt@NiO$_x$, Pt@CuO$_x$, and Pt(111) catalysts, the step of NO$_2$ formation has the largest X_{RC} value, indicating that NO$_2$ formation is the rate-controlling step. Although the different rate limiting steps in

Table 4
Rate-controlling step and reaction rates (r) for NO oxidation reactions at Pt (111) and Pt@TMO catalysts determined by DFT calculations.

Catalysts	r(s^{-1})	Rate-controlling step
Pt@MnO$_x$	5.47E-02	NO$_2$*MnO*Pt ↔ NO$_2$ + MnO*Pt
Pt@FeO$_x$	9.01E-03	NO$_2$*FeO*Pt ↔ NO$_2$ + FeO*Pt
Pt@CoO$_x$	2.44E+00	NO$_2$*CoO*Pt ↔ NO$_2$ + CoO*Pt
Pt@NiO$_x$	6.26E-01	NO*O*NiO*Pt ↔ NO$_2$*NiO*Pt
Pt@CuO$_x$	5.02E-01	NO*O*CuO*Pt ↔ NO$_2$*CuO*Pt
Pt(111)	3.11E-03	NO*O*O*Pt ↔ NO$_2$*O*Pt

different catalysts, the steps of NO$_2$ formation and desorption play an important role in soot oxidation subsequently. As shown in Table 4, Pt@CoO$_x$ model shows the largest reaction rate (r, 2.44 s^{-1}) for NO oxidation, followed by the models of Pt@NiO$_x$ (r = 6.26 × 10^{-1} s^{-1}), Pt@CuO$_x$ (r = 5.02 × 10^{-1} s^{-1}), Pt@MnO$_x$ (r = 5.47 × 10^{-2} s^{-1}), Pt@FeO$_x$ (r = 9.01 × 10^{-3} s^{-1}), and bare Pt(111) surface (r = 3.11 × 10^{-3} s^{-1}). It indicates that the activities of supported Pt@TMO core-shell catalysts are higher than that of bare Pt(111) catalyst, and the active sites located at the interface of core-shell structured Pt@CoO$_x$ model has the highest catalytic activity for NO oxidation in comparison with other TMOs. From the above, supported Pt@TMO core-shell nanoparticle catalysts can improve the catalytic activity for NO oxidation, and supported Pt@CoO$_x$ catalyst shows the strongest property for enhancing formation of NO$_2$, which is in accord with the results of NO-TPO and soot-TPO.

4.4. Catalytic mechanism for soot oxidation

The above results and discussions indicate that the catalysts consisting of both Pt core and TMO shell as active components possess the strong redox ability and good catalytic performances for soot oxidation. Based on the results of soot-TPO tests and DFT calculations, the catalytic pathways of Pt@TMO/3DOM-Al$_2$O$_3$ catalysts for soot oxidation are described below, and schematic diagram is displayed in Fig. 10.

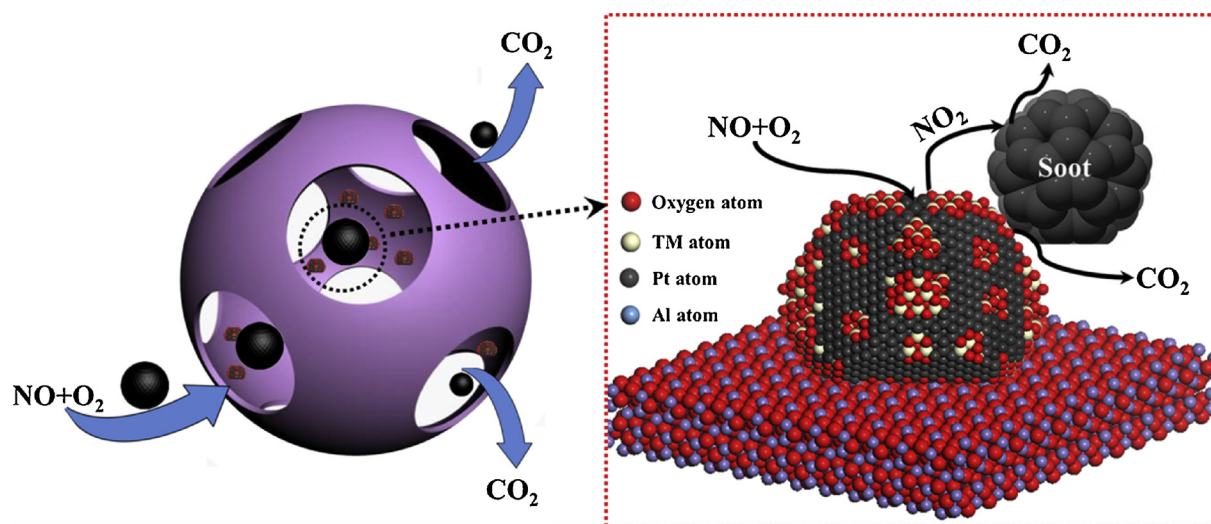**Fig. 10.** Schematic diagram of the Pt@TMO/3DOM-Al$_2$O$_3$ catalysts for soot combustion.

First, the novel nanocatalysts of Pt@TMO (TM: Mn, Fe, Co, Ni, Cu) core-shell nanoparticles supported on 3DOM Al$_2$O$_3$ were successfully fabricated using the GBMR/P method. 3DOM structure can enhance the contact efficiency of soot-catalysts and the mass transfer of "soot-flow" through the porous interior with the help of a reactant gas; thus, the catalytic activity can be improved when the catalytic pathway is direct (catalyst-O$_a$-soot) or indirect (catalyst-O$_a$-NO-NO$_2$-soot) due to the shortening of the reaction distance between the soot and catalysts. Second, Pt@TMO core-shell nanoparticles over 3DOM-Al$_2$O$_3$ can increase the density of active sites located at the interfaces of strong Pt-TMO interaction for adsorption-activation of O$_2$ and NO. The oxidation capability of active sites is strongly dependent on the Pt-TMO interaction, which is an intrinsic property in improving the catalytic activity for soot oxidation. Among supported Pt@TMO core-shell nanoparticles, the coordination unsaturated Co active sites at the Pt-CoO$_x$ interface have efficient catalytic performance on NO oxidation to NO$_2$ as an intermediate oxidant in comparison with other TMOs. Finally, active oxygen species and NO$_2$ at the Pt-TMO interface can migrate to the surface of diesel soot particles and can oxidize them to CO$_2$ via the indirect pathway (NO + 1/2O$_2$→NO$_2$ and NO$_2$ + soot→CO$_2$). Therefore, Pt@CoO$_x$/3DOM-Al$_2$O$_3$ catalyst shows the highest catalytic activity (T_{50} = 357 °C) and the lowest apparent activation energies (52 kJ mol^{-1}) for soot oxidation.

5. Conclusions

3DOM Al$_2$O$_3$ support was successfully prepared by CCT method, and a series of core-shell structured Pt@TMO/3DOM-Al$_2$O$_3$ catalysts were synthesized by GBMR/P method. The periodic voids of 270–320 nm in 3DOM structure are interconnected via the pore window (85 ± 5 nm). Pt@TMO core-shell nanoparticles are highly dispersed on the inner walls of 3DOM-Al$_2$O$_3$ support. The sizes of Pt core have a narrow distribution in the range 3–7 nm, while the thicknesses of TMO shell layers are 2–6 nm. The strong interaction between Pt core and TMO shell is favorable for improving redox property and for increasing amount of surface active oxygen species. Pt@TMO/3DOM-Al$_2$O$_3$ catalysts exhibit super catalytic activity for diesel soot oxidation in contrast to Pt/3DOM-Al$_2$O$_3$ catalyst, and their catalytic activities dependent on the strong Pt-TMO interaction. Among Pt@TMO/3DOM-Al$_2$O$_3$ catalysts, Pt@CoO$_x$/3DOM-Al$_2$O$_3$ catalyst exhibits the highest catalytic activity for soot oxidation in the presence of O$_2$ (5%), NO (0.2%) and H$_2$O (5%), i.e., its T_{50} value and $S_{CO_2}^m$ are 352 °C and 98.2%, respectively, its highest activity (TOF) is 2.76 S^{-1} ×10^{-3} and the lowest Ea value is only 52 kJ mol^{-1}. Pt@TMO/3DOM-Al$_2$O$_3$ catalysts

have also excellent H$_2$O and SO$_2$ resistances during catalytic soot oxidation. Based on the results of characterizations and DFT calculations, it is proved that the indirect path (NO$_2$-assisted mechanism) is an absolutely dominant position for soot oxidation, and the coordination unsaturated Co active sites at the Pt-CoO$_x$ interface are favorable for the formation of active oxygen species for NO oxidation to NO$_2$, which is the rate-determining step for soot oxidation. In summary, the work not only suggests a new route for Pt@TMO core-shell nanoparticles with strong Pt-TMO interactions to significantly improve its catalytic performance for diesel soot oxidation, but also provides a strategy to synthesize novel uniform nanostructured catalysts, which is useful in the design of high-performance catalytic nanomaterials.

Appendix A. Supplementary data

Supplementary material related to this article can be found, in the online version, at doi:https://doi.org/10.1016/j.apcatb.2018.11.094.

References

[1] C. Su, Y. Wang, A. Kumar, P.J. McGinn, Catalysts 8 (2018) 247.
[2] Y. Kuwahara, A. Fujibayashi, H. Uehara, K. Mori, H. Yamashita, Catal. Sci. Technol. 8 (2018) 1905–1914.
[3] J. Xiong, Q. Wu, X. Mei, J. Liu, Y. Wei, Z. Zhao, D. Wu, J. Li, ACS Catal. 8 (2018) 7915–7930.
[4] H. Wang, B. Jin, H. Wang, N. Ma, W. Liu, D. Weng, X. Wu, S. Liu, Appl. Catal. B 237 (2018) 251–262.
[5] L. Nossova, G. Caravaggio, M. Couillard, S. Ntais, Appl. Catal. B 225 (2018) 538–549.
[6] S. Wagloehner, J.N. Baer, S. Kureti, Appl. Catal. B 147 (2014) 1000–1008.
[7] V. Rico-Pérez, E. Aneggi, A. Bueno-López, A. Trovarelli, Appl. Catal. B 197 (2016) 95–104.
[8] H. Lin, S. Li, H. He, Z. Wu, J. Wu, L. Chen, D. Ye, M. Fu, Appl. Catal. B 223 (2018) 91–102.
[9] F. Ji, Y. Men, J. Wang, Y. Sun, Z. Wang, B. Zhao, X. Tao, G. Xu, Appl. Catal. B 242 (2019) 227–237.
[10] K. Mori, Y. Iwata, M. Yamamoto, N. Kimura, A. Miyauchi, G. Okamoto, T. Toyoshima, H. Yamashita, J. Phys. Chem. C 118 (2014) 9078–9085.
[11] C. Cao, L. Xing, Y. Yang, Y. Tian, T. Ding, J. Zhang, T. Hu, L. Zheng, X. Li, Appl. Catal. B 218 (2017) 32–45.

[12] W.Y. Hernández, D. Lopez-Gonzalez, S. Ntais, C. Zhao, A. Boréave, P. Vernoux, Appl. Catal. B 226 (2018) 202–212.

[13] F. Fang, N. Feng, L. Wang, J. Meng, G. Liu, P. Zhao, P. Gao, J. Ding, H. Wan, G. Guan, Appl. Catal. B 236 (2018) 184–194.

[14] S. Liu, X. Wu, D. Weng, M. Li, J. Fan, Appl. Catal. B 138-139 (2013) 199–211.

[15] T. Andana, M. Piumetti, S. Bensaid, L. Veyre, C. Thieuleux, N. Russo, D. Fino, E.A. Quadrelli, R. Pirone, Appl. Catal. B 226 (2018) 147–161.

[16] A. Serve, A. Boreave, B. Cartoixa, K. Pajot, P. Vernoux, Appl. Catal. B 242 (2019) 140–149.

[17] T. Liu, Q. Li, Y. Xin, Z. Zhang, X. Tang, L. Zheng, P.X. Gao, Appl. Catal. B 232 (2018) 108–116.

[18] D. Jampaiah, V.K. Velisoju, P. Venkataswamy, V.E. Coyle, A. Nafady, B.M. Reddy, S.K. Bhargava, ACS Appl. Mater. Interfaces 9 (2017) 32652–32666.

[19] V.D. Sarli, G. Landi, L. Lisi, A. Saliva, A.D. Benedetto, Appl. Catal. B 197 (2016) 116–124.

[20] E. Aneggi, D. Wiater, C. Leitenburg, J. Llorca, A. Trovarelli, ACS Catal. 4 (2014) 172–181.

[21] Y. Wei, J. Liu, Z. Zhao, A. Duan, G. Jiang, C. Xu, J. Gao, H. He, X. Wang, Energy Environ. Sci. 4 (2011) 2959–2970.

[22] C. Cao, X. Li, Y. Zha, J. Zhang, T. Hu, M. Meng, Nanoscale 8 (2016) 5857–5864.

[23] X. Wang, Y. Zhang, Q. Li, Z. Wang, Z. Zhang, Catal. Sci. Technol. 2 (2012) 1822–1824.

[24] M. Sadakane, T. Horiuchi, N. Kato, C. Takahashi, W. Ueda, Chem. Mater. 19 (2007) 5779–5785.

[25] V. Alcalde-Santiago, A. Davó-Quiñonero, D. Lozano-Castelló, A. Bueno-López, Appl. Catal. B 234 (2018) 187–197.

[26] K. Leistner, C.G. Braga, A. Kumar, K. Kamasamudram, L. Olsson, Appl. Catal. B 241 (2019) 338–350.

[27] J.H. Kwak, J. Hu, D. Mei, C.W. Yi, D.H. Kim, C.H.F. Peden, L.F. Allard, J. Szanyi, Science 325 (2009) 1670–1673.

[28] H. He, X. Lin, S. Li, Z. Wu, J. Gao, J. Wu, W. Wen, D. Ye, M. Fu, Appl. Catal. B 223 (2018) 134–142.

[29] F. Hu, Y. Peng, J. Chen, S. Liu, H. Song, J. Li, Appl. Catal. B 240 (2019) 329–336.

[30] Y. Wei, X. Wu, Y. Zhao, L. Wang, Z. Zhao, X. Huang, J. Liu, J. Li, Appl. Catal. B 236 (2018) 445–457.

[31] Q. Fu, W.X. Li, Y. Yao, H. Liu, H. Su, D. Ma, X. Gu, L. Chen, Z. Wang, H. Zhang, B. Wang, X. Bao, Science 328 (2010) 1141–1144.

[32] S. Zhang, L. Nguyen, J.X. Liang, J. Shan, J.J. Liu, A.I. Frenkel, A. Patlolla, W. Huang, J. Li, F.F. Tao, Nat. Commun. 6 (2015) 7938.

[33] Y. Wei, J. Liu, Z. Zhao, Y. Chen, C. Xu, A. Duan, G. Jiang, H. He, Angew. Chem. Int. Ed 50 (2011) 2326–2329.

[34] G.N. Vayssilov, Y. Lykhach, A. Migani, T. Staudt, G.P. Petrova, N. Tsud, T. Skála, A. Bruix, F. Illas, V. Matolín, K.M. Neyman, J. Libuda, Nat. Mater. 10 (2011) 310–315.

[35] J.M. Yan, X.B. Zhang, T. Akita, M. Haruta, Q. Xu, J. Am. Chem. Soc. 132 (2010) 5326–5327.

[36] M. Cargnello, J.J. Delgado Jaén, J.C. Hernández Garrido, K. Bakhmutsky, T. Montini, J.J. Calvino Gámez, R.J. Gorte, P. Fornasiero, Science 337 (2012) 713–717.

[37] Q. Dai, S. Bai, Y. Lou, X. Wang, Y. Guo, G. Lu, Nanoscale 8 (2016) 9621–9628.

[38] Y. Wei, Z. Zhao, J. Liu, C. Xu, G. Jiang, A. Duan, Small 9 (2013) 3957–3963.

[39] Y. Wei, J. Jiao, Z. Zhao, J. Liu, J. Li, G. Jiang, Y. Wang, A. Duan, Appl. Catal. B 179 (2015) 422–432.

[40] C. Lee, J.I. Park, Y.G. Shul, H. Einaga, Y. Teraoka, Appl. Catal. B 174-175 (2015) 185–192.

[41] Z. Chen, Y. Mao, J. Chen, H. Wang, Y. Li, P. Hu, ACS Catal. 7 (2017) 4281–4290.

[42] R. Li, H. Li, J. Liu, Int. J. Quantum Chem. 116 (2016) 908–914.

[43] H. Arandiyan, H. Dai, J. Deng, Y. Liu, B. Bai, Y. Wang, X. Li, S. Xie, J. Li, J. Catal. 307 (2013) 327–339.

[44] M. Piumetti, S. Bensaid, N. Russo, D. Fino, Appl. Catal. B 165 (2015) 742–751.

[45] N. An, Q. Yu, G. Liu, S. Li, M. Jia, W. Zhang, J. Hazard. Mater. 186 (2011) 1392–1397.

[46] Y. Kobayashi, J. Horiguchi, S. Kobayashi, Y. Yamazaki, K. Omata, D. Nagao, M. Konno, M. Yamada, Appl. Catal. A Gen. 395 (2011) 129–137.

[47] Y. Wei, Z. Zhao, T. Li, J. Liu, A. Duan, G. Jiang, Appl. Catal. B 146 (2014) 57–70.

[48] S. Xie, J. Deng, S. Zang, H. Yang, G. Guo, H. Arandiyan, H. Dai, J. Catal. 322 (2015) 38–48.

[49] S. Xie, Y. Liu, J. Deng, X. Zhao, J. Yang, K. Zhang, Z. Han, H. Arandiyan, H. Dai, Appl. Catal. B 206 (2017) 221–232.

[50] F. Teng, M. Chen, G. Li, Y. Teng, T. Xu, Y. Hang, W. Yao, S. Santhanagopalan, D.D. Meng, Y. Zhu, Appl. Catal. B 110 (2011) 133–140.

[51] Y. Wei, J. Jiao, X. Zhang, B. Jin, Z. Zhao, J. Xiong, Y. Li, J. Liu, J. Li, Nanoscale 9 (2017) 4558–4571.

[52] J. Oi-Uchisawa, A. Obuchi, Z. Zhao, S. Kushiyama, Appl. Catal. B 18 (1998) 183–187.

[53] C. Davies, K. Thompson, A. Cooper, S. Golunski, S.H. Taylor, M.B. Macias, O. Doustdar, A. Tsolakis, Appl. Catal. B 239 (2018) 10–15.

[54] Y. Wei, J. Liu, Z. Zhao, A. Duan, G. Jiang, Appl. Catal. A Gen. 453 (2013) 250–261.